Numerical Investigation of Supersonic Dense-Gas Boundary Layers

Luca Sciacovelli, Donatella Passiatore, Xavier Gloerfelt, Paola Cinnella, Francesco Grasso

Numerical investigation of supersonic dense-gas boundary layers

Luca Sciacovelli[1], Donatella Passiatore[1], Xavier Gloerfelt[1], Paola Cinnella[1], and Francesco Grasso[2]

[1] Arts et Métiers ParisTech, DynFluid Laboratory, Paris 75013, France,
[2] Conservatoire National des Arts et Métiers, DynFluid Laboratory, Paris, France
luca.sciacovelli@ensam.eu

Abstract. A study of dense-gas effects on the laminar, transitional and turbulent characteristics of boundary layer flows is conducted. The laminar similarity solution shows that temperature variations are small due to the high specific heats of dense gases, leading to velocity profiles close to the incompressible ones. Nevertheless, the complex thermodynamics of the base flow has a major impact on unstable modes, which bear similarities with those obtained for a strongly cooled wall. Numerical simulations of spatially developing boundary layers yield turbulent statistics for the dense gas flow that remain closer to the incompressible regime than perfect gas ones despite the presence of strongly compressible structures.

Keywords: dense gas, boundary layers, numerical simulations

1 Introduction

Dense gases are single-phase fluids, of medium to high molecular complexity, that can exhibit non-classical phenomena when working at thermodynamic conditions close to their liquid/vapor critical point. The study of dense-gas flows is strongly motivated by their use in several engineering systems, such as high-Reynolds wind tunnels, chemical transport and processing, refrigeration and energy conversion cycles. The potential advantages of their use as working fluid in Organic Rankine Cycles is drawing increasing interest from both the industrial and academic communities [1]. Considerable progress has been made in the past 30 years on dense gas flows. Such flows have been extensively studied analytically, with focus on the generation of non-classical compressibility effects like expansion shocks, sonic and double-sonic shocks, and shock splitting [2–4]. More recently, Direct Numerical Simulations (DNS) have been carried out with the aim to assess the influence of dense-gas effects on compressible isotropic turbulence [5, 6] as well as turbulent channel flows [7] configurations. Nevertheless, reliable experimental measurements are still difficult to obtain. To this purpose, high-fidelity datasets, as those provided by DNS, represent an effective tool for getting insight into the physics of turbulent dense-gas flows and for the assessment of lower-fidelity models [8].

In this work, we discuss the properties of supersonic boundary layers (BL) of a dense gas in the laminar, transitional and turbulent regimes, with special

focus on the latter. The aim is multifold as the complex behaviour of the gas is expected to have a predominant role in altering classically observed perfect-gas features for each of the three regimes. To this purpose, a generalized laminar compressible Blasius solution for zero-pressure gradient BL of fluids governed by an arbitrary equation of state (EoS) is derived and analyzed first. Then, elements of linear stability are used to shed some light on the laminar-to-turbulent transition mechanism. Finally, the turbulent regime is investigated by means of quasi-direct numerical simulations. This allows the extraction of useful engineering information (such as heat transfer at the wall, friction coefficient, ..) and represents a first step towards high-fidelity simulations for configurations of industrial interest, such as turbine flows.

2 Governing equations

We consider flows of gases in the single-phase regime, governed by the compressible Navier–Stokes equations. The selected working fluid is PP11 (commercial name of perfluoro-perhydrophenanthrene, $C_{14}F_{24}$), a heavy fluorocarbon that has been extensively studied in the past because of its wide inversion zone, and for which DNS data exist [6, 7]. The thermodynamic behaviour of PP11 is modeled by the Martin–Hou EoS [9] and the variation of the transport properties with temperature and density is described by means of the Chung–Lee–Starling dense-gas model [10]. The dense gas is compared to air, modeled as a perfect gas and assuming Sutherland law and constant Prandtl number to determine its transport properties.

3 Laminar regime

The similarity solution for a zero-pressure-gradient laminar BL has been extended to fluids governed by an arbitrary EoS. A generalized coordinate transformation is applied to the governing equations by means of the definition of the similarity variables

$$\xi = \rho_\infty \mu_\infty U_\infty x = \xi(x), \qquad \eta = \frac{U_\infty}{\sqrt{2\xi}} \int_0^y \rho \, \mathrm{d}y = \eta(x, y) \tag{1}$$

with x and y the streamwise and wall-normal directions, respectively, and where the subscript $(\cdot)_\infty$ represents free-stream conditions. The transformation leads to the following system of two ordinary differential equations in the variable η:

$$\begin{cases} (c\, f_{\eta\eta})_\eta + f\, f_{\eta\eta} = 0 \\ f\, g_\eta + \left(\frac{c}{\mathrm{Pr}} g_\eta\right)_\eta + c\,\mathrm{Ec}\, f_{\eta\eta}^2 = 0 \end{cases} \tag{2}$$

where $f{=}f(\eta)$, $g{=}g(\eta)$ and $(\cdot)_\eta$ represents a derivative with respect to η, being $f_\eta{=}u/U_\infty$, $g{=}h/h_\infty$, $\mathrm{Pr} = \mu c_p/k$ the Prandtl number, $\mathrm{Ec} = U_\infty^2/h_\infty$ the Eckert number and $c = \rho\mu/\rho_\infty\mu_\infty$ the Chapman-Rubesin parameter. The functions f and g are subject to the boundary conditions:

$$f(0) = 0, \quad f_\eta(0) = 0, \quad f_\eta(\infty) = 1, \quad g_\eta(0) = 0, \quad g(\infty) = 1. \tag{3}$$

The system is solved by means of the multi-dimensional Broyden shooting method.

First, the influence of the Mach number is investigated for both air and PP11. The reference thermodynamic conditions for air are fixed to $T_\infty = 65\,\mathrm{K}$ and $\rho_\infty = 0.1298\,\mathrm{kg/m^3}$. For PP11, the conditions are set to $T_\infty = 0.995T_c(= 646.9\,\mathrm{K})$ and $\rho_\infty = 0.6\rho_c(= 376.47\,\mathrm{kg/m^3})$, corresponding to a negative value of the fundamental derivative of gas dynamics, $\Gamma = -0.217$.

Figure 1 shows the distribution of the velocity profiles for air and PP11 for different Mach numbers, as a function of the incompressible-transformed variable $\eta_{\mathrm{inc}} = y/\sqrt{\frac{\nu x}{U_\infty}}$ and the compressible one η. As the Mach number grows, the perfect-gas BL thickens considerably; this is due the increase in viscosity, which in turn is a direct consequence of the BL friction heating. Concerning PP11, on the contrary, the velocity profiles are quite insensitive to the Mach number and to the compressible scaling: this is due to the high molecular complexity (high heat capacity) of this fluid, for which kinetic energy conversion into heat by viscous friction leads to much smaller temperature variations and, as a consequence, smaller variations of other thermodynamic and transport properties. Specifically, while the deviation of wall thermodynamic quantities (shown in figure 2) with respect to the external state increases with M_∞ for both fluids, variations of T and ρ in the dense gas are much smaller. Furthermore, the viscosity profile of the dense gas has an opposite evolution compared to the perfect one, and closely follows the density profile. Note that a similar behaviour was observed for channel flows configurations [7].

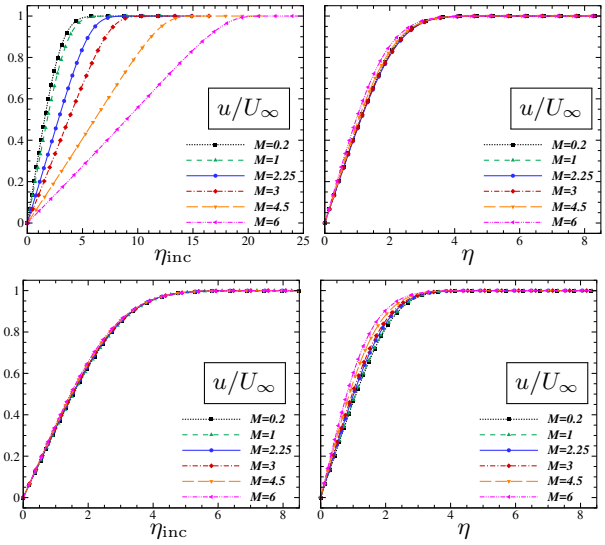

Fig. 1. Velocity profiles as a function of the incompressible (left) and compressible (right) transformed variable η for air (top) and PP11 (bottom).

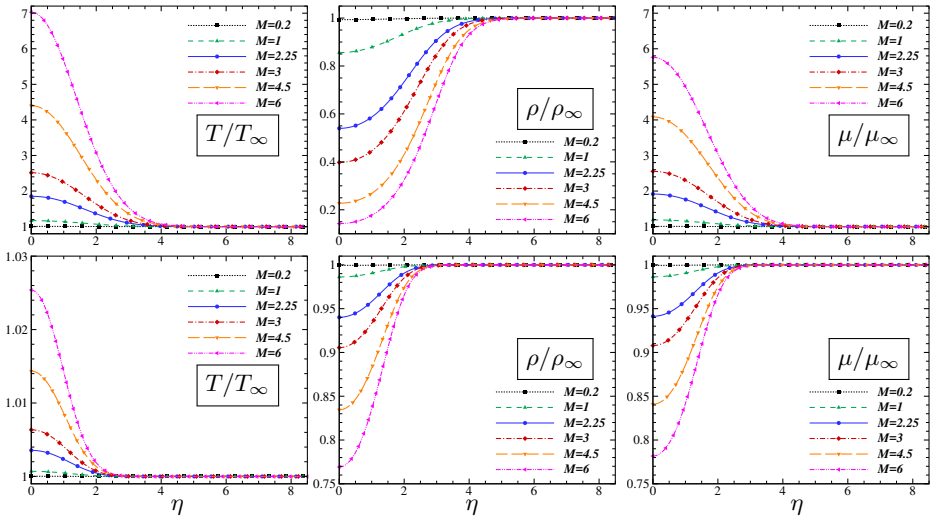

Fig. 2. Profiles of temperature (left), density (center) and viscosity (right), normalized with respect to outer variables, at various Mach numbers. Air (top) and PP11 (bottom).

A parametric study of the effect of the thermodynamic operating conditions for PP11 (not reported for brevity) shows qualitatively similar behaviours for a range of external pressures and temperatures lying close to the saturation curve and characterized by values of the fundamental derivative of gas dynamics lower than one, including cases with $\Gamma < 0$. This indicates that the specific heat at constant pressure and, to a minor extent, the density dependent viscosity are the leading parameters governing the BL behaviour for the dense gas. Nonclassical gas dynamic effects do not play any role in such a smooth flow.

4 Stability analysis

With the aim of triggering turbulence via a modal laminar-to-turbulent transition scenario, Linear Stability Theory (LST) was used to determine the most unstable modes for both the perfect- and dense-gas BLs. The base flow is given by the similarity solver and three-dimensional spatial modes are searched with a real angular frequency ω and a complex wavenumber $\boldsymbol{k} = \alpha \boldsymbol{e}_x + \beta \boldsymbol{e}_z$. The streamwise component of the wavenumber is $\alpha = \alpha_r + i\alpha_i$, where α_i represents the amplification rate and β is the real transverse wavenumber. The results are made nondimensional using U_∞ as the velocity scale and $L^* = \sqrt{\nu x / U_\infty}$ as rhe length scale. The nondimensional frequency is defined as $\omega = \frac{2\pi f L^*}{U_\infty}$. The perfect-gas results, reported in figure 3a, are in agreement with the literature. Specifically, we chose the operating conditions of Ma and Zhong [11] for a quantitative validation (not reported) of the present LST calculations. For air, at low Mach numbers, the flow exhibits a viscous unstable mode (Tollmien-Schlichting mode) for $\omega \simeq 0.03$. As the Mach number becomes supersonic (see the close-up view in figure 4a) the most unstable wave is skewed, with a wave angle $\psi = \arctan(\beta/\alpha_r)$

of about 37° (figure 4b). The growth rate of this so-called "first" mode is progressively reduced by compressibility. However, at higher Mach numbers this effect is counterbalanced by the appearance of a generalized inflection point (defined as the point where $\frac{\partial}{\partial y}\left(\rho\frac{\partial u}{\partial y}\right) = 0$), so that the nature of the mode becomes more and more inviscid. For Mach numbers between 4 and 5, a so-called "second" mode appears, as described by Mack [12]. This is sometimes qualified as an "acoustic" mode, due to the presence of acoustic waves trapped between the wall and the relative sonic line. At hypersonic conditions the second mode is dominant. LST results for PP11 are reported in figure 3b, which provides a global view for Mach numbers in the range $[0.5, 6]$ and freestream thermodynamic conditions $\rho_\infty = 348.41\,\mathrm{kg/m^3}$ and $T_\infty = 646.83\,\mathrm{K}$. For low Mach numbers, the first mode behaves similarly to the perfect gas case. Inspection of the close-up view of figure 4c shows that both the frequency and the growth rate are similar to the perfect-gas ones at $M = 0.5$. For higher Mach numbers, the mode is damped by compressibility and is preferentially skewed (e.g., see figure 4d for $M = 1.5$). However, due to the much weaker density variation, no generalized inflection point is created. As a consequence, no inviscid inflectional effects appear to counteract compressibility stabilization, and the first mode becomes stable for Mach numbers above approximately 2.5. For the case $M = 2.25$, of interest for the present simulations, the first mode is totally stable in 2D and becomes slightly unstable in 3D, for high values of the wave angle ($\sim 67°$). Beyond Mach 3, the only unstable mode is the second mode, visible in figure 3b. This appears at higher frequencies than in air, due to the reduced thickness of the dense gas BL. Such mode is also of acoustic nature and, due to the supersonic values reached by its phase speed, it might spontaneously radiate acoustic waves. Radiating supersonic modes have been described for high-enthalpy non-equilibrium perfect-gas BLs with highly-cooled walls [13, 14]. The modified nature of the second mode is related to the drastic reduction of friction heating in the dense gas, which in turn is mostly related to the fluid molecular complexity, non-ideal gas and transport-property effects playing only a secondary role. A more detailed discussion about dense gas LST results will be the object of an upcoming paper.

5 Numerical simulation

Numerical experiments of the flat plate BL at $M_\infty = 2.25$ are carried out using a Cartesian computational domain. The grid is evenly spaced in the streamwise (x) and spanwise (z) directions and stretched in the wall-normal (y) one. An in-house finite-difference code is used to solve the governing equations described in section 2. The inviscid fluxes are discretized by means of tenth-order standard centered differences; the scheme is supplemented with a non-linear artificial viscosity term containing a Ducros-type sensor, making it ninth-order-accurate far from discontinuities. Viscous fluxes are discretized with standard fourth-order centered derivatives. A classical four-step Runge–Kutta algorithm is used for time integration. At the inflow, the compressible laminar solution generated by the similarity code is imposed. Isothermal no-slip conditions are applied at the wall, with a temperature close to the laminar adiabatic wall temperature.

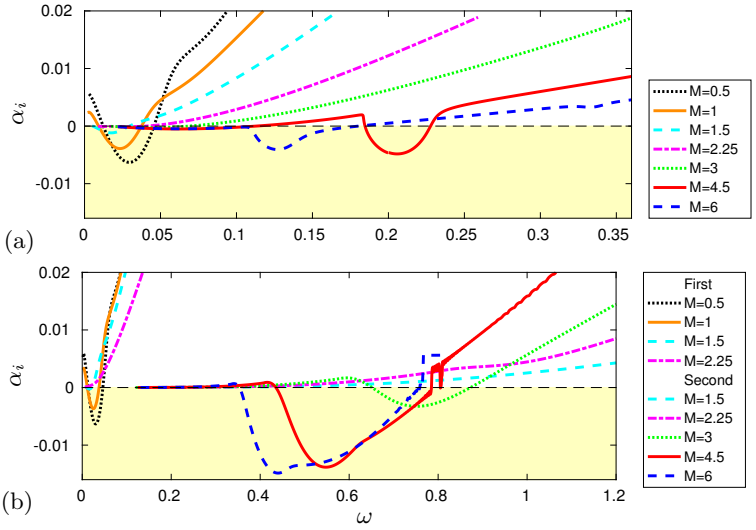

Fig. 3. Influence of Mach number on LST growth rate for air (a) and PP11 (b).

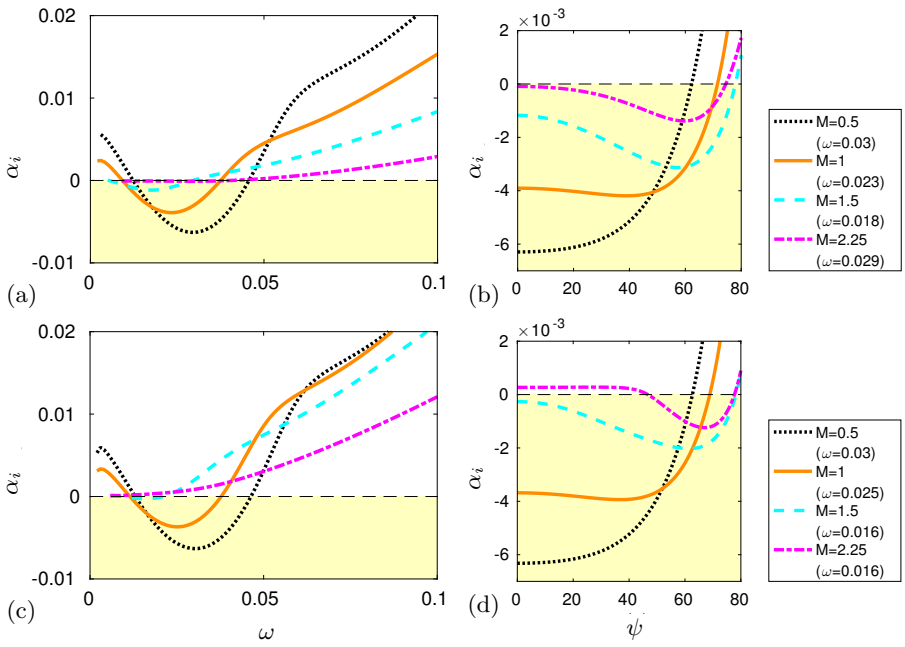

Fig. 4. Air top, PP11 bottom. On the left, close-up view at low frequencies of the LST 2D growth rate. On the right, evolution of the maximal amplification rate as a function of the wave angle ψ for a fixed frequency (given in parentheses).

Characteristics-based boundary conditions are imposed at the outflow, and periodic conditions are applied in the spanwise direction. Transition to turbulence is achieved by means of a suction and blowing forcing [15]. A time-and-space dependent wall-normal velocity is imposed at the wall in a small region downstream of the inlet:

$$v_w = f(x)g(z)\sum_{n=1}^{N_{\text{mode}}} A_n \sin(\omega_n t - \beta_n z) \text{ with } \begin{cases} f(x) = e^{-\frac{x-x_0}{2\sigma^2}} \\ g(z) = 1 + 0.1\left[e^{-\left(\frac{z-z_w}{z_w}\right)^2} - e^{-\left(\frac{z+z_w}{z_w}\right)^2}\right] \end{cases}$$

where A_n, ω_n and β_n are the amplitude, the pulsation and the spanwise amplitude of the n-th mode, respectively; $\sigma^2 = 0.87\frac{2\pi U_\infty}{\omega\delta^*_{\text{forc}}}$ (δ^*_{forc} being the displacement thickness at the forcing location, chosen as reference length) and z_w is chosen based on the domain width. Of note, the spanwise domain length L_z is fixed as to contain an integer-valued number of wavelengths λ, $L_z = 2\pi\lambda/\beta$.
Based on the LST results, the setup of the dense-gas and air cases differs from each other. For the perfect-gas simulation, two oppositely-oriented oblique first mode instability waves are introduced, with a normalized pulsation $\omega\delta^*_{\text{forc}}/U_\infty = 0.12$. The normalized spanwise wave-number and amplitude are set to $\beta\delta^*_{\text{forc}}$=0.2 and A/U_∞=0.01, respectively. For PP11, since no 2D unstable mode was found, a series of numerical tests was performed in order to identify a suitable set of forcing parameters at an arbitrarily chosen position (*i.e.* $\text{Re}_{\delta^*_{\text{forc}}}$). Following a similar methodology as for the air case, two oppositely-oriented oblique modes are introduced with $\omega\delta^*_{\text{forc}}/U_\infty$=0.6, A/U_∞=0.035 and $\beta\delta^*_{\text{forc}}$=0.3; additionally, a set of smaller disturbances are superposed to the primary one. This excitation leads to a bypass-type abrupt transition. A summary of the numerical parameters and of the reference conditions are reported in table 1. The computational grids chosen allow to achieve good resolutions, that are DNS-like for the perfect gas and slightly coarser in the x and z directions for the dense gas. Given the good near-wall resolution, the latter simulation can be categorized as a wall-resolved implicit LES. The following study will focus on global and first-order quantities, whose profiles are less sensitive to grid resolution and can be safely analysed both qualitatively and quantitatively.

Several results extracted from reference data available in literature (listed in table 2) are considered for the dual purpose of assessing the quality of the air simulation and highlighting the differences with respect to PP11.

The evolution of the integral quantities is first evaluated. Figure 5a shows the distribution of the skin friction coefficient C_f as a function of the momentum-thickness-based Reynolds number Re_θ. While the present results for air compare rather well to perfect-gas data from the literature, this is not the case for PP11. A striking difference is represented by the higher range of Re_θ achieved for the dense gas. It is useful to project the data in the "incompressible plane", by means of the Van Driest II transformation:

$$C_{f,\text{inc}} = \frac{\overline{T}_w/T_\infty - 1}{\arcsin^2\alpha} C_f \quad \text{with} \quad \alpha = \frac{\overline{T}_w/T_\infty - 1}{\sqrt{\overline{T}_w/T_\infty(\overline{T}_w/T_\infty - 1)}}, \tag{4}$$

Table 1. Reference conditions, domain size, number of points, grid resolution and forcing parameters used for the air and PP11 numerical simulations.

	Air	PP11
M_∞	2.25	2.25
ρ_∞	$0.1298\,\mathrm{kg/m^3}$	$348.4\,\mathrm{kg/m^3}$
$T_\infty - T_w$	$65\,\mathrm{K} - 120.18\,\mathrm{K}$	$650.8\,\mathrm{K} - 653.4\,\mathrm{K}$
$L_x/\delta^*_{\mathrm{forc}}$	2162	1930
$L_y/\delta^*_{\mathrm{forc}}$	51	38
$L_z/\delta^*_{\mathrm{forc}}$	16	10.5
$N_x \times N_y \times N_z$	$4000 \times 210 \times 140$	$10000 \times 270 \times 176$
$\Delta_x^+ \times \Delta_y^+ \times \Delta_z^+$	$11.57 \times 0.82 \times 5.63$	$19.57 \times 0.98 \times 12.07$
$\mathrm{Re}_{\delta^*,\mathrm{in}}$	1700	3000
$\mathrm{Re}_{\delta^*,\mathrm{forc}}$	2000	3100
$\mathrm{Re}_{\theta,\mathrm{trans}}$	1400	2000
$\mathrm{Re}_{\theta,\mathrm{exit}}$	4600	9200
$\omega\delta^*_{\mathrm{forc}}/U_\infty$	0.12	see table on the right
$\beta\delta^*_{\mathrm{forc}}$	0.2	
A/U_∞	0.01	

ω_n^*	β_n^*	A_n/U_∞
0.6	± 0.3	0.0350
0.6	± 0.6	0.0018
0.6	± 1.2	0.0018
0.6	± 1.8	0.0018
0.6	± 2.4	0.0018
0.6	± 6.0	0.0018

Table 2. Legend for current simulations (lines) and reference data (symbols).

		M_∞	$\mathrm{Re}_{\theta,\mathrm{exit}}$
—	Air simulation	2.25	4600
—	PP11 simulation	2.25	9200
○	[16] Pirozzoli & Bernardini (2011)	2.0	1242, 2921, 6071
◇	[17] Wenzel et al. (2018)	2.0, 2.5	≈ 2100, ≈ 2200
▽	[18] Pirozzoli et al. (2004)	2.25	4263
◁	[19] Martin (2004)	2.32	4452
▼	[20] Schlatter & Örlü (2010)	0	4300
■	[21] Spalart (1988)	0	1410

and using the incompressible Reynolds number $\mathrm{Re}_{\theta,\mathrm{inc}} = \frac{\mu_\infty}{\overline{\mu}_w}\mathrm{Re}_\theta$. This widely employed transformation enables the comparison with well-established incompressible correlations and data from the literature [16]. The evolution of $C_{f,\mathrm{inc}}$ is shown in figure 5b. In this case, we find a good agreement for PP11 with respect to both reference data and incompressible prediction. Interestingly, the "overshoot" in the values of the skin friction coefficient and the heat transfer, classically observed in transition to turbulence for compressible flows, is not obtained for PP11, denoting a behaviour closer to the incompressible one. Similar considerations hold for the shape factor and the friction Reynolds number, shown in figures 5c-d. For the air case, the distributions of both quantities lie between the predictions of Wenzel et al. [17] for $M_\infty = 2$ and 2.5, and they agree well with the results of the temporal DNS of Martin [19]. For PP11, again, the behaviour is much closer to the incompressible evolution as shown by the much smaller shape factor and the proximity to the (Re_τ-$\mathrm{Re}_{\theta,\mathrm{inc}}$) correlation proposed by Schlatter & Örlü [20].

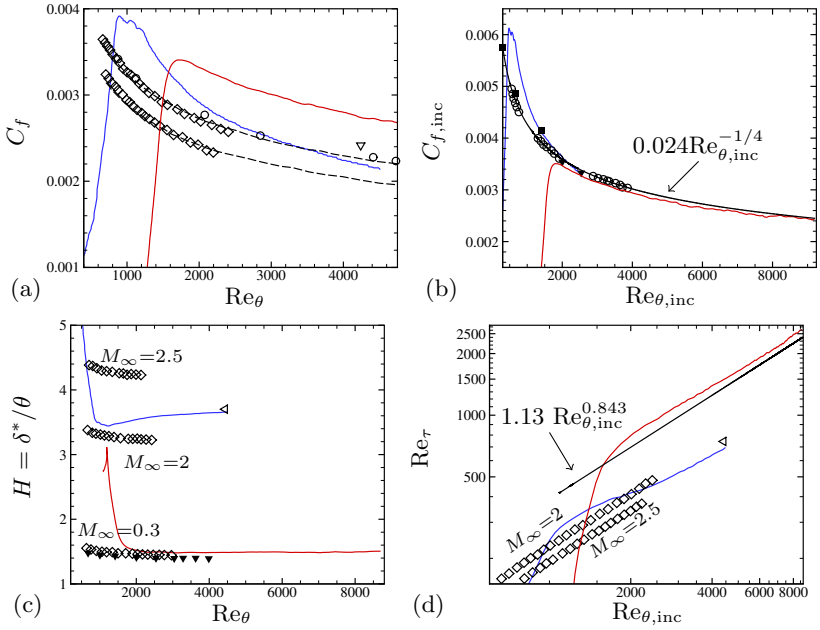

Fig. 5. Evolution of C_f as a function of Re_θ (a); $C_{f,\mathrm{inc}}$ as a function of $\mathrm{Re}_{\theta,\mathrm{inc}}$ (b); the shape factor H as a function of Re_θ (c) and the friction Reynolds number Re_τ as a function of $\mathrm{Re}_{\theta,\mathrm{inc}}$ (d). Lines and symbols as in table 2. In panel (b), the black solid line denotes an incompressible correlation, whereas the black dashed lines in panel (a) are the compressible counterparts at M=2 and M=2.5. The black solid line in panel (d) denotes the incompressible correlation of Schlatter & Örlü [20].

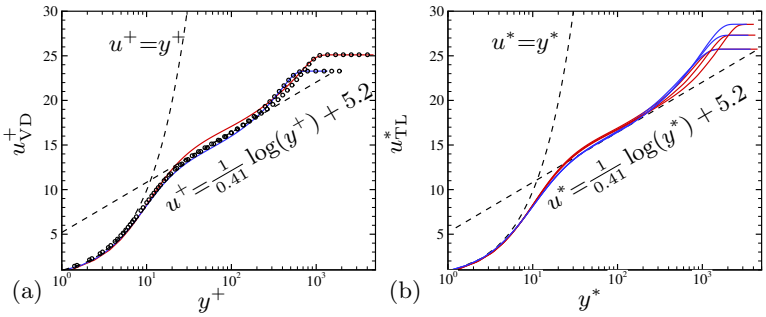

Fig. 6. Distribution of the transformed velocity profiles: incompressible Van-Driest scaling at $\mathrm{Re}_\tau = 580$ (a) and compressible Trettel-Larsson scaling at three different friction Reynolds numbers (b). Lines and symbols as in table 2.

In figure 6 we report the transformed velocity profiles. Two different transformations are considered; namely, the classical density-scaled Van Driest transformation (u_{VD}), and the Trettel-Larsson transformation (u_{TL}) [22] that takes into account the wall-normal viscosity variation:

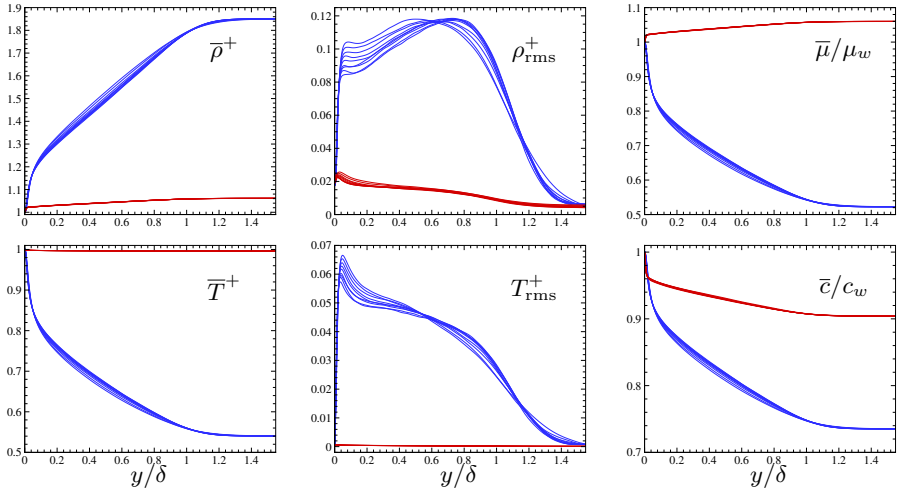

Fig. 7. Profiles of different thermodynamic quantities for air and PP11 at ten different stations across the TBL. Lines as in table 2.

$$u_{\mathrm{VD}} = \int_0^{\bar{u}} \sqrt{\frac{\overline{\rho}}{\overline{\rho}_w}}\,\mathrm{d}u, \qquad u_{\mathrm{TL}} = \int_0^{\bar{u}} \sqrt{\frac{\overline{\rho}}{\overline{\rho}_w}}\left[1 + \frac{1}{2}\frac{1}{\overline{\rho}}\frac{\mathrm{d}\overline{\rho}}{\mathrm{d}y}y - \frac{1}{\overline{\mu}}\frac{\mathrm{d}\overline{\mu}}{\mathrm{d}y}y\right]\mathrm{d}u. \tag{5}$$

The latter has proven to be successful in collapsing dense-gas velocity profiles for supersonic turbulent channel flows [7]. For air, the Van-Driest-transformed velocity profile is able to scale correctly the profiles up to the logarithmic region. Results are superposed to reference data [16], extracted at $\mathrm{Re}_\tau = 580$. For PP11, u_{VD} follows closely the non-transformed profile because of the weaker variations of density (approximately one order of magnitude smaller than the air case, see figure 7). Some differences are observed in the outer region. The Trettel-Larsson scaling slightly improves the predictions for both air and PP11, but it is not as effective as for variable-property channel flows, being unable to scale the wake region properly. The nearly incompressible behaviour of the skin friction and velocity profiles was previously observed in [23] by using the Reynolds-Averaged equations supplemented by a turbulence model.

Given the different range of characteristic Reynolds numbers in which the two TBLs evolve, profiles of thermodynamic quantities are shown in figure 7 at ten different stations across the turbulent sections. The distributions confirm the trend observed in the laminar similarity solution, namely, larger wall-normal and streamwise variations for air. Temperature variations in PP11 are negligible, whereas viscosity profiles essentially follow the density ones, with an opposite trend with respect to air. This behaviour may heavily affect the scaling for the velocity profiles and the Reynolds stresses. The average value of Γ increases across the BL, reaching a positive maximum at the wall: this is due to the small temperature increase with respect to the edge value. Nevertheless, a large extent

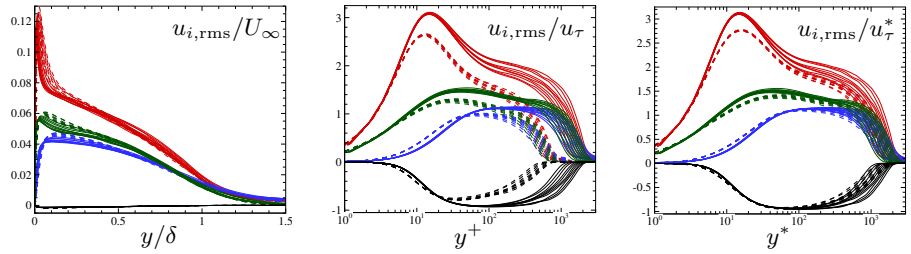

Fig. 8. Similarity profiles of the rms velocities and Reynolds shear stress at ten different streamwise locations across TBL in outer units (left panel) and inner units (middle and right panels). Solid lines, PP11; dashed lines, air; ● u_{rms}; ● v_{rms}; ● w_{rms}; ● $u'v'$.

of the upper BL evolves in the $\Gamma < 0$ area. Inspection of the turbulent Mach number distribution shows that its peak value is sufficiently small ($M_{t,\max} < 0.3$) to prevent the creation of eddy shocklets, so that non-classical BZT phenomena are not expected to occur at the considered conditions. Further investigations are in progress. Figure 8 shows the three different scaling laws tested for the Reynolds stresses; specifically, an outer scaling based on edge quantities, an incompressible inner scaling based on wall quantities, and the density-weighted semi-local scaling (where u_τ^* is the semi-local density-scaled friction velocity defined as $u_\tau^* = \sqrt{\tau_w/\overline{\rho}}$). The outer scaling works effectively in the outer region but the collapse in the inner region is lost. Due to the weak wall-normal variation of the averaged density, the incompressible- and semi-local scaled profiles are almost superposed for PP11. The semi-local scaling is much more effective for air, contributing to bring the profiles closer to PP11 and to obtain a correspondence in the wall-normal location of the peaks. Nevertheless, large deviations remain, especially for the streamwise stress.

6 Conclusion

Dense gas laminar and turbulent boundary layers have been analyzed by means of linear stability theory and numerical simulations. On the one hand, laminar flow analyses (based on the extension of the compressible Blasius solution for zero-pressure-gradient boundary layers to fluids governed by an arbitrary EoS) show that, due to strong decoupling of the dynamic and thermal boundary layers: i) velocity profiles remain close to the incompressible ones up to very high values of the external Mach number; ii) the temperature changes are limited to less than 3% throughout the flow; and iii) the transport properties exhibit an opposite variation with respect to the one observed in perfect gases (*e.g.*, viscosity follows a trend similar to density and decreases when approaching the plate wall). Secondly, the influence of dense gas effects on modal transition scenarios has been analyzed by a spatial linear stability analysis. Due to the high values of the specific heat coefficient of dense gases, the boundary layer stability is deeply altered with respect to that of a perfect gas at the same Mach number, and is reminiscent of the behaviour of strongly cooled supersonic and hyper-

sonic boundary layers. Finally, turbulent boundary layer numerical simulations have been carried out for PP11 and air at $M_\infty = 2.25$. Transition is induced by means of a suction and blowing excitation, whose characteristics have been chosen with the guidance of the preceding stability analysis. At the chosen M_∞, no 2D unstable modes were found for PP11, hence a large-disturbance bypass mechanism is used to trigger transition. The results obtained for the fully turbulent flow region show that turbulent statistics (integral, thermodynamic and dynamic quantities) of dense gas flows are also found to remain closer to the incompressible regime than perfect gas ones. Further investigation is being carried out for the scaling of velocity profiles and Reynolds stresses, and to understand the impact of dense gas effects on the dynamics of turbulent structures.

Acknowledgments

This work was granted access to the HPC resources of IDRIS and TGCC under the allocation 2018-7332 made by GENCI (Grand Equipement National de Calcul Intensif). We also acknowledge TGCC for awarding us access to the Joliot-Curie supercomputer under the allocation "Grands Challenges" gch032.

References

1. P. Colonna, E. Casati, C. Trapp, T. Mathijssen, J. Larjola, T. Turunen-Saaresti, A. Uusitalo, Journal of Engineering for Gas Turbines and Power **137**(10), 100801 (2015)
2. P. Thompson, K. Lambrakis, Journal of Fluid Mechanics **60**(01), 187 (1973)
3. M. Cramer, A. Kluwick, Journal of Fluid Mechanics **142**, 9 (1984)
4. M. Cramer, Nonlinear waves in real fluids pp. 91–145 (1991)
5. L. Sciacovelli, P. Cinnella, C. Content, F. Grasso, Journal of Fluid Mechanics **800**(1), 140 (2016)
6. L. Sciacovelli, P. Cinnella, F. Grasso, Journal of Fluid Mechanics **825**, 515 (2017)
7. L. Sciacovelli, P. Cinnella, X. Gloerfelt, Journal of Fluid Mechanics **821**, 153 (2017)
8. L. Sciacovelli, P. Cinnella, X. Gloerfelt, Flow, Turbulence and Combustion **101**(2), 295315 (2018)
9. J. Martin, Y. Hou, AIChE Journal **1**(2), 142 (1955)
10. T. Chung, L. Lee, K. Starling, Industrial & Engineering Chemistry Fundamentals **23**(1), 8 (1984)
11. Y. Ma, X. Zhong, Journal of Fluid Mechanics **488**, 31 (2003)
12. L. Mack, Boundary-layer linear stability theory. Tech. rep., California Institute of Technology - Jet Propulsion Laboratory (1984)
13. N. Bitter, J. Shepherd, Journal of Fluid Mechanics **778**, 586 (2015)
14. P. Chuvakhov, A. Fedorov, Journal of Fluid Mechanics **805**, 188 (2016)
15. K. Franko, S. Lele, Journal of Fluid Mechanics **730**, 491 (2013)
16. S. Pirozzoli, M. Bernardini, Journal of Fluid Mechanics **688**, 120 (2011)
17. C. Wenzel, B. Selent, M. Kloker, U. Rist, Journal of Fluid Mechanics **842**, 428 (2018)
18. S. Pirozzoli, F. Grasso, T. Gatski, Physics of Fluids **16**(3), 530 (2004)
19. P. Martin, in *34th AIAA Fluid Dynamics Conference and Exhibit* (2004), p. 2337
20. P. Schlatter, R. Örlü, Journal of Fluid Mechanics **659**, 116 (2010)
21. P.R. Spalart, Journal of fluid mechanics **187**, 61 (1988)
22. A. Trettel, J. Larsson, Physics of Fluids **28**(2), 026102 (2016)
23. P. Cinnella, P. Congedo, Journal of Fluid Mechanics **580**, 179 (2007)